Journal of Alloys and Compounds 879 (2021) 160345

Contents lists available at ScienceDirect

Journal of Alloys and Compounds

journal homepage: www.elsevier.com/locate/jalcom

Review

In situ study of the process of formation of hexagonal $NiSi_2$ nanoplates and spherical Ni nanoparticles embedded in a Si(001) wafer covered by a Ni-doped SiO_2 thin film

Daniel da Silva Costa[a,*], Guinther Kellermann[a], Aldo F. Craievich[b], Lisandro J. Giovanetti[c], Cristián Huck-Iriart[d], Félix G. Requejo[c]

[a] Department of Physics, University Federal of Paraná, Curitiba, PR, Brazil
[b] Institute of Physics, University of São Paulo, São Paulo, Brazil
[c] Instituto de Investigaciones Fisicoquímicas Teóricas y Aplicadas (INIFTA, Fac. Ciencias Exactas, UNLP/CONICET), CC/16 suc. 4, 1900 La Plata, Argentina
[d] Laboratorio de Cristalografía Aplicada, Escuela de Ciencia y Tecnología (ECyT), Universidad Nacional de San Martín (UNSAM), 1650, San Martin, Buenos Aires, Argentina

ARTICLE INFO

Article history:
Received 21 January 2021
Received in revised form 4 May 2021
Accepted 7 May 2021
Available online 13 May 2021

Keywords:
GISAXS
Hexagonal nanoplates
Kinetic of growth

ABSTRACT

We have studied for the first time the relevant features of the thermally activated nanostructural transformations occurring in a material initially consisting of a flat Si(001) wafer in which a nanoporous Ni-doped silica film is deposited. Two simultaneous transformation processes occur, and both were investigated by *in situ* grazing-incidence small-angle X-ray scattering during isothermal annealing at 405 °C, namely the kinetics of formation of (i) oriented $NiSi_2$ hexagonal nanoplates endotaxially buried in a Si(001) wafer, and (ii) a set of randomly oriented spherical Ni nanocrystals with a two-mode radius distribution embedded in a Ni-doped silica thin film deposited on the Si wafer and in an intermediate layer between SiO_2 film and the layer in which $NiSi_2$ nanoplates are embedded. The analyses of the successive 2D scattering patterns measured *in situ* during isothermal annealing led us to establish the time invariances of the average radii of the spherical Ni nanocrystals and the time dependence of their number, together with the time dependences of the maximum diameter, thickness, number and total volume of the hexagonal $NiSi_2$ nanoplates buried in the Si wafer.

Contents

1. Introduction

Transition metals silicides such as $NiSi_2$ exhibit high electrical conductivity and are structurally stable at high temperatures. As

* Corresponding author.
E-mail address: daniel.costa@ufpr.br (D. da Silva Costa).

https://doi.org/10.1016/j.jallcom.2021.160345
0925-8388/

demonstrated in a previous article [1] the isothermal annealing of a composite consisting of a flat Si(001) wafer covered by Ni-doped silica thin film promotes the formation and growth of highly oriented $NiSi_2$ hexagonal nanoplates buried inside and near the surface of the Si(001) wafer. Moreover, since the crystalline lattices of $NiSi_2$ and Si are both cubic and their lattice parameters are very close ($\Delta a/a$ = 0.4% at 20 °C), their interfaces become coherently related. The high electrical conductivity and structural stability of $NiSi_2$, the well-defined orientation of the $NiSi_2$ nanoplates grown in Si wafers and the coherence of the Si/$NiSi_2$ interface together with the possibility of using known silicon miniaturization procedures make the Si/$NiSi_2$ composites good candidates for different nanotechnological devices, such as field effect transistors for nanoelectronics [2–4] and thermoelectric thin films [5–7].

In a previous investigation, a sample consisting of a Si(001) wafer covered by a nanoporous Ni-doped SiO_2-based thin film was subjected to a thermal annealing at 500 °C during 40 min and then studied *ex situ*, at room temperature, by scanning transmission electron microscopy (STEM), high-resolution scanning transmission electron microscopy (HR-STEM), atomic force microscopy (AFM), X-ray reflectometry (XRR) and grazing-incidence small-angle X-ray scattering (GISAXS) [1].

Our analyses of different experimental STEM images and GISAXS patterns revealed the presence of two types of nanoparticles embedded in the studied samples [1]:

(i) thin hexagonal nanoplates embedded in a Si wafer and located close to but not in contact with the wafer external surface having their larger surface parallel to one of the lattice planes of the Si {111} crystallographic form. The thin hexagonal nanoplates were demonstrated to be $NiSi_2$ single crystals with their lattices coherently related to the lattice of the host Si single crystalline wafer, and
(ii) nearly spherical nanoparticles embedded in a deposited SiO_2 film and inside an intermediate layer located between the nanoporous SiO_2 thin film and the layer in the Si wafer that contains the $NiSi_2$ nanoplates. The analysis of HR-STEM images of an earlier article [1] demonstrated that the observed nearly spherical nanoparticles are Ni nanocrystals.

The intermediate layer between the SiO_2 thin film and the layer in which $NiSi_2$ nanoplates are located exhibits a Si based structure with a very irregular morphology, which is due to corrosion effects produced by a preliminary HF etching procedure to which the wafer is subjected. Corrosion effects led to a very high roughness of the Si surface, as it was also shown by X-ray reflectometry measurements [1].

In order to obtain $NiSi_2$ nanoplates embedded in a Si wafer, in a previous study and in that to be reported here, a novel procedure was used [1]. This preparation procedure promotes the direct formation of $NiSi_2$ nanoplates embedded in the Si wafer. In this method, Ni atoms diffuse from the Ni-doped SiO_2 thin film into the Si wafer and react with Si atoms of the host wafer and build up $NiSi_2$ thin nanoplates.

In the present work, we have conducted an *in situ* GISAXS study during an isothermal annealing at 405 °C of a sample initially consisting of a single-crystalline Si(001) wafer covered by a SiO_2-based thin film. Our GISAXS results allowed us to characterize the processes of formation and growth of (i) $NiSi_2$ nanoplates buried in a Si (001) wafer with their large faces parallel to the Si{111} crystallographic planes and (ii) Ni nanoparticles embedded in a thin Ni-doped SiO_2 film and inside the Si(001) wafer close to its external surface. The temperature of isothermal annealing (405 °C) was selected to be somewhat lower than that previously used (500 °C) [1]. This choise avoided a too fast nanoparticle growth thus favoring the statistical quality of the results of our *in situ* GISAXS study of the structural transformation process.

The sample studied here was held at constant high temperature while successive GISAXS patterns were recorded. In this way, the analyses of a number of experimental GISAXS patterns led us to characterize (i) the time dependences of the total volume, shape and sizes of the Ni nanoparticles and (ii) the time dependences of the shape, orientation, number and sizes of the hexagonal $NiSi_2$ nanoplates.

2. Experimental method

2.1. Sample preparation

A 1 × 1 cm^2 Si(001) wafer was embedded in acetone using a ultrasonic bath at room temperature during 15 min and subsequently using a concentrated HSO_4 solution at 80 °C (97%, Merck) during 15 min to remove organic contaminants. The native silicon oxide was removed from the Si wafer by etching with a concentrated solution of HF (48%, Merck) during 1 min. The sample was finally dried under a N_2 gas flow.

The thin film deposited on the surface of the Si(001) wafer was prepared using a sol-gel procedure consisting of two successive depositions of different precursor solutions using the spin-coating technique. The precursor liquid solution for the first deposition step was composed of 0.15 g of $Ni(NO_3)_26H_2O$ (99,999%, Sigma-Aldrich) in 1.15 g of isopropyl alcohol (98%, Merck). For the second deposition step, the precursor consisted of 0.05 g of tetraethoxysilane (TEOS) (99,999%, Sigma-Aldrich) and 0.30 g of HNO_3 (65%, Merck) in 0.90 g of isopropyl alcohol (98%, Merck). TEOS, HNO_3 and isopropyl alcohol were mixed and kept at room temperature during 1 day before being deposited on the Si wafer in order to promote chemical reactions and a densification process leading to the formation of a SiO_2-based gel. In order to suppress volatiles and reduce the Ni oxide in the thin film on the Si(001) substrate, the wafer covered by the thin film was held during 40 min at 300 °C under 50 sccm flow rate of $5H_2$ + 95He gas mixture at 1 atm.

The two-step deposition process here used, in which the solution containing the Ni precursor was directly deposited on the Si wafer, is expected to increase the Ni concentration near surface of the wafer. However a partial interdiffusion between these two layers, due to the redissolution of $Ni(NO_3)_26H_2O$ during TEOS plus isopropanol deposition, may occur thus leading to a concentration gradient of Ni in direction perpendicular to the sample surface. Thus, the final sample to be studied by GISAXS consists of a flat Si(001) single crystalline wafer covered by a nanoporous Ni-doped SiO_2 thin film.

2.2. Setup for in situ GISAXS measurements at high temperature

The GISAXS measurements were performed at the XRD2 beam line of the Brazilian Synchrotron Radiation Laboratory (LNLS) using a specially designed high temperature electrical furnace [8]. The setup for thermal annealing and recording of a series of 2D GISAXS patterns during the whole isothermal annealing of the sample is shown in Fig. 1. The measurements of 2D GISAXS patterns were performed *in situ* every 60 s during thermal annealing at 405 °C. The 2D patterns of GISAXS intensity were recorded using a Pilatus 300 K detector with 172×172 μm^2 pixel size. The wavelength of the primary X-ray beam was λ = 0.15495 nm and the sample-to-detector distance was 395.2 mm. To account for smearing effects on GISAXS patterns due to the non-zero cross-section of the incident beam, the modeling function to be defined in Section 3 was convoluted with a 2D Gaussian function before fitting to experimental results. The width and height parameters of the Gaussian function are Δq_y = 0.14 nm^{-1} and Δq_z = 0.08 nm^{-1}, respectively.

The grazing-incidence angle between the primary X-ray beam and the sample surface was adjusted to α_i = 0.36°. This angle was experimentally determined by optimizing the conditions that

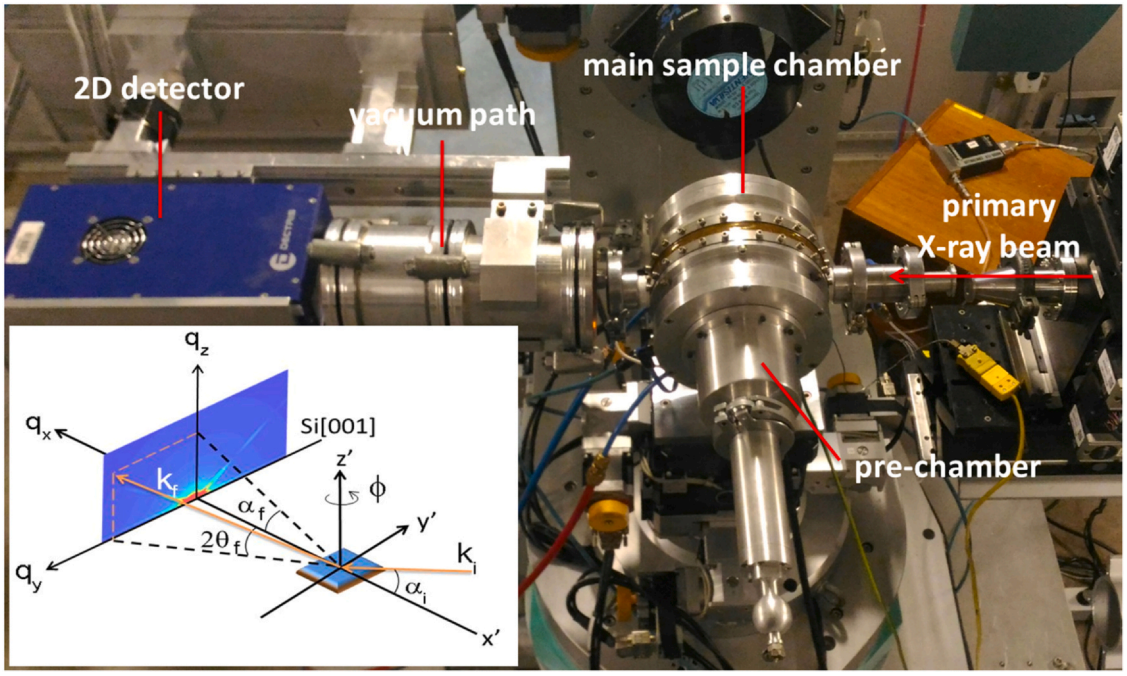

Fig. 1. Experimental setup used for *in situ* measurements of GISAXS patterns at high temperature. Inset: Relevant geometrical parameters for analysis of the results of GISAXS experiments.

allowed us to maximize the scattering intensity and reach an adequate penetration depth of X-rays in the sample. The specific mass and thickness of the nanoporous Ni-doped SiO_2 thin film determined in previous measurements by X-ray reflectometry and transmission electron microscopy (TEM), respectively were 0.19 g/cm^3 and 85 nm, respectively [1]. Under the conditions described above and taking in consideration the compositions, specific masses, film thickness, X-ray wavelength and incident angle, our calculations determined a decrease of 11.8% in the intensity of the incident X-ray beam after crossing the Ni-doped SiO_2 film and becomes equal to 1/e of its maximum value after reaching a depth of 388 nm from the sample surface. The penetration depths were calculated as described in [9]. Details are given in Sec. A of Supplementary Material (SM).

A previous investigation [1] in which a sample prepared using a similar method was studied *ex situ*, after thermal annealing, revealed that beside the growth of Ni nanocrystals inside the SiO_2 thin film, other Ni nanocrystals are formed in a ~85 nm thick layer located close to the Si(001). Thus, the intensity of the probing (incident) X-ray beam was above 1/e of its value at the external surface of the thin film along the whole sample depth in which Ni nanocrystals and $NiSi_2$ nanoplates were embedded.

A vacuum-path with Kapton windows was placed between the sample chamber and the 2D-detector in order to reduce the X-ray scattering intensity by air. The continuous decrease in intensity of the X-ray beam produced by the synchrotron radiation source was monitored with a scintillation detector that recorded the decreasing X-ray scattering intensity produced by a thin Mylar film placed in the path of the primary X-ray beam.

The studied sample was held at a constant temperature (T = 405 °C) by using an electrical heater placed inside the sample chamber equipped with a precise control system. While heating the chamber up to the annealing temperature, the sample was placed inside a pre-chamber kept at room temperature. When the final temperature of isothermal annealing was reached, a translation stage placed the sample into the main chamber. This procedure allowed a fast heating of the sample and prevented overheating effects. The sample temperature was recorded by using a type-K calibrated thermocouple. The uncertainty in the temperature of the sample was estimated to be ±1 °C. In order to avoid the re-oxidation of Ni atoms in the Ni-doped thin film during the *in situ* GISAXS experiment, the sample was kept under constant He flow at a rate of 200 sccm slightly above the atmosphere pressure.

The series of GISAXS measurements started immediately after the sample was inserted into the furnace thus allowing for recording GISAXS patterns from early stages of the formation and growth of Ni nanocrystals and $NiSi_2$ nanoplates. The recorded 2D GISAXS patterns were analyzed as functions of the scattering vector $\vec{q}$, given by:

$$\begin{pmatrix} q_x \\ q_y \\ q_z \end{pmatrix} = \frac{2\pi}{\lambda} \begin{pmatrix} cos\,\alpha_f\, cos\,2\theta_f - cos\,\alpha_i \\ cos\,\alpha_f\, sin\,2\theta_f \\ sin\,\alpha_f + sin\,\alpha_i \end{pmatrix} \quad (1)$$

where α_i and α_f are the angles of the sample surface with the primary and scattered X-ray beams, respectively. The horizontal scattering angle $2\theta_f$ is defined in the inset of Fig. 1.

3. Modeling of GISAXS patterns

The modeling of the GISAXS patterns was based on the results of a previous investigation [1] which were summarized in the Introduction section. The total GISAXS intensity was modeled by a function that contains two independent contributions to the total scattering intensity, namely (i) a isotropic 2D pattern produced by spherical Ni nanocrystals growing in the SiO_2 thin film and inside an intermediate layer, and (ii) an anisotropic 2D pattern with a shape of narrow diagonal "leaves" produced by hexagonal $NiSi_2$ nanoplates endotaxially buried in the single-crystalline Si host, each of them having their large surfaces parallel to one of the four planes of the Si {111} crystallographic form [1].

A preliminary analysis of *in situ* GISAXS results suggested the presence of Ni nanoparticles with bimodal size distribution and oriented $NiSi_2$ nanoplates. The size distributions of smaller and larger nanoparticles were labeled as mode 1 and mode 2, respectively. The preliminary analysis of the results of our *in situ* GISAXS study indicated the growth in the number of nanoparticles of each mode without significant variation in their size. This preliminary

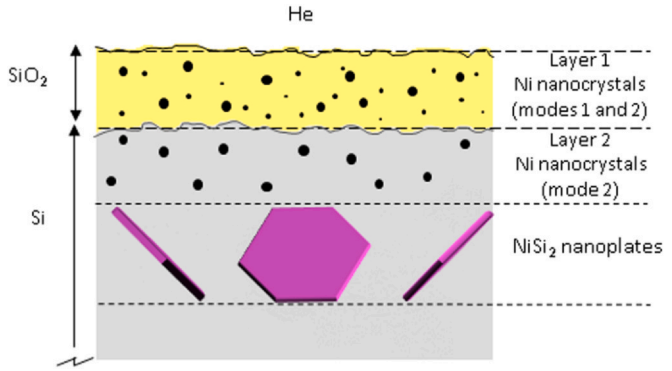

Fig. 2. Schematical structure model consisting of two layers in which Ni nanocrystals are embedded and a 3rd layer in which $NiSi_2$ nanoplates are located. On the left, the matrices in the three layers are indicated.

result and those corresponding to a previous investigation [1] led us to model the GISAXS intensity based on the structure schematically shown in Fig. 2, in which we can notice that mode 1 nanoparticles are formed inside the SiO_2-based thin film (layer 1), mode 2 nanoparticles are embedded in the thin film (layer 1) and in an intermediate layer (layer 2) and the $NiSi_2$ nanoplates are deeply buried inside the Si(001) wafer (layer 3). Furhermore, the shapes of the spherical Ni nanocrystals and $NiSi_2$ nanoplates were considered to be preserved along the whole growth process.

In our modeling of the GISAXS equation, we have not included the effects produced by the Si/SiO_2 interface on the reflections of X-ray beams scattered by nanoparticles embedded in the thin film and those buried in the Si substrate (i. e. in the intermediate layer). This assumption was based on (i) previous AFM results showing that both the silicon wafer surface after HF etching and the top surface of the Ni-doped SiO_2 film were highly rough and (ii) the results from X-ray reflectivity experiments showing that the internal interface roughness leads to a strong decrease in reflectivity [1]. In the case of very rough interfaces these reflection effects could be safely disregarded [10] (see Sec. B in SM).

Under the assumptions described above and considering that the nanoparticles are randomly located in each layer, the total GISAXS intensity can be written as:

$$I(q,t) \propto |T(\alpha_i)|^2 |T(\alpha_f)|^2 \left\{ \int_{R=0}^{\infty} \left(\tfrac{4}{3}\pi R^3\right)^2 \left|F_{sph}(q_{||}, \tilde{q}_z, R)\right|^2 \times \left[\frac{(\rho_{Ni}-\rho_{SiO_2})^2}{A_1} N_{sph(1)}(R,t) + \left(c\frac{(\rho_{Ni}-\rho_{SiO_2})^2}{A_1} + (1-c)\frac{(\rho_{Ni}-\rho_{Si})^2}{A_2} \right) N_{sph(2)}(R,t) \right] dR + \frac{(\rho_H-\rho_{Si})^2}{A_3} \frac{1}{4} \sum_{i=1}^{4} \int_{\delta=0}^{\infty} \left|H_i[\alpha, \phi, q_{||}, \tilde{q}_z', D(t), \delta(t)]\right|^2 N_{thick}(\delta, t) d\delta \right\} \quad (2)$$

where $T(\alpha_i)$ and $T(\alpha_f)$ are the Fresnel transmission functions of the incident and scattered beams through the SiO_2/air interface, respectively, $F_{sph}(R)$ is the normalized scattering amplitude of a spherical nanoparticle of radius R, $H_i(D, \delta)$ are the scattering amplitudes due to the regular hexagons with maximum lateral diameter $D(t)$ and thickness $\delta(t)$, $N_{thick}(\delta, t)d\delta$ is the number of $NiSi_2$ nanoplates with thickness values in the δ and $\delta + d\delta$ range, $N_{sph(1)}(R, t)dR$ and $N_{sph(2)}(R, t)dR$ are the number of Ni nanospheres with radius values in the R and range for populations (1) and (2), respectively, c is the number fraction of the larger (mode 2) Ni nanoparticles in SiO_2 thin film, A_1 and A_2 are the factors that account for the attenuations of the intensity for Ni particles embedded in SiO_2 and in the intermediary layer, respectively, and A_3 is the attenuation of intensity for $NiSi_2$ platelets buried in Si. The procedure used to calculate A_1, A_2 and A_3 is described in Sec. A of SM. The electron densities ρ_{Ni}, ρ_{SiO_2}, ρ_H and ρ_{Si} corresponds to Ni, SiO_2, $NiSi_2$ and Si, respectively, $q_{||} = \sqrt{q_x^2 + q_y^2}$, $\tilde{q}_z$ and $\tilde{q}_z{}'$ are the components of the horizontal scattering vector in the z direction inside the thin film and Si wafer, and α_i, α_f and ϕ are defined in the inset of Fig. 1. α is the angle between the surface of the wafer and the Si(100) crystallographic planes. The H_i and F_{sph} functions are included in SM. The subscript i (i = 1–4) in H_i refers to the four possible orientations of the nanohexagons in the Si host matrix (assumed them to be equally probable) having their largest surface parallel to one of the four planes of the Si{111} crystallographic form. Gaussian and lognormal functions were assumed for the dispersion in thickness of $NiSi_2$ nanoplates and for the radius distribution of the spherical Ni nanocrystals, respectively (see SM).

Our modeling of the GISAXS intensity assumes that the lateral maximum diameters $D(t)$ of all hexagonal $NiSi_2$ nanoplates at a given annealing time have the same value. Even though the platelets may exhibit some narrow dispersion in D values, the Eq. (2) model is still expected to hold thus giving average values for $D(t)$. The reasonability of this assumption will be demonstrated later on.

The electron density of the Ni-doped SiO_2 matrix of the SiO_2 thin film is a priori expected to vary during the growth of the Ni nanoparticles and $NiSi_2$ nanoplates. However, considering that the electron density of the thin SiO_2 film ρ_{SiO_2} remains much lower than the density of metallic Ni nanoparticles ρ_{Ni} over the whole process, we assumed that the diffence $(\rho_{Ni} - \rho_{SiO_2})$ remains approximately invariant. For similar reasons, the electron density contrasts between Ni nanoparticles and $NiSi_2$ and their matrices in the intermediate layer and Si wafer, respectively, were also considered as time invariants.

Based on the arguments of the precedent paragraph, we have assumed in Eq. (2) that the attenuations, A_1, A_2 and A_3, are time independent over the whole process. These values are also considered to be space independent within each layer, which is a reasonable approximation as described in Supplementary Material.

4. Experimental results

Fig. 3(a) to (d) (left column) display a series of selected $(q_{||}, q_z)$ 2D-GISAXS patterns recorded *in situ*, at 405 °C, at the indicated annealing times. The formation of Ni nanoparticles is evidenced by a strong isotropic scattering intensity and the $NiSi_2$ nanoplates by a weak intensity with leaf-like shapes pointing perpendicularly to Si{111} crystallographic planes. As a priori expected, we can notice in Fig. 3 that the thin leaves of GISAXS intensity associated to the $NiSi_2$ nanoplates displayed in the $(q_{||}, q_z)$ plane are not symmetric with respect to $q_{||} = 0$. This effect occurs because the primary X-ray beam was not precisely aligned with the Si[110] crystallographic direction (Fig. 1). We have included this geometrical feature by adding an adjustable azimuthal angle ϕ in Eq. (2) that accounts for an eventual sample misalignment. A value $\phi = 1.0$ degrees was derived from the best fit of Eq. (2) to the experimental GISAXS intensity profiles.

The 2D GISAXS patterns displayed on the right side of Fig. 3 (Fig. 3e to h) are the 2D $(q_{||}, q_z)$ patterns calculated by using Eq. (2) with the structure parameters derived from the best fit to the experimental 1D GISAXS profiles displayed in Fig. 4(a) to (d). We notice a good visual agreement of the simulated 2D GISAXS patterns displayed in Fig. 3(e) to (h) with those corresponding to the experimental patterns displayed in Fig. 3(a) to (d).

The curves indicated by symbols in Fig. 4(a) to (d) are a series of four 1D $(I \times q_{||})$ GISAXS intensity profiles for different q_z values derived from the patterns displayed in Fig. 3(a) to (d). Moreover, the continuous lines in Fig. 4(a) to (d) are the functions given by Eq. (2) that best fit to the experimental profiles. The good fit of Eq. (2) to 1D GISAXS experimental scattering functions for all selected annealing times confirms that the shape of the Ni nanocrystals and the shape

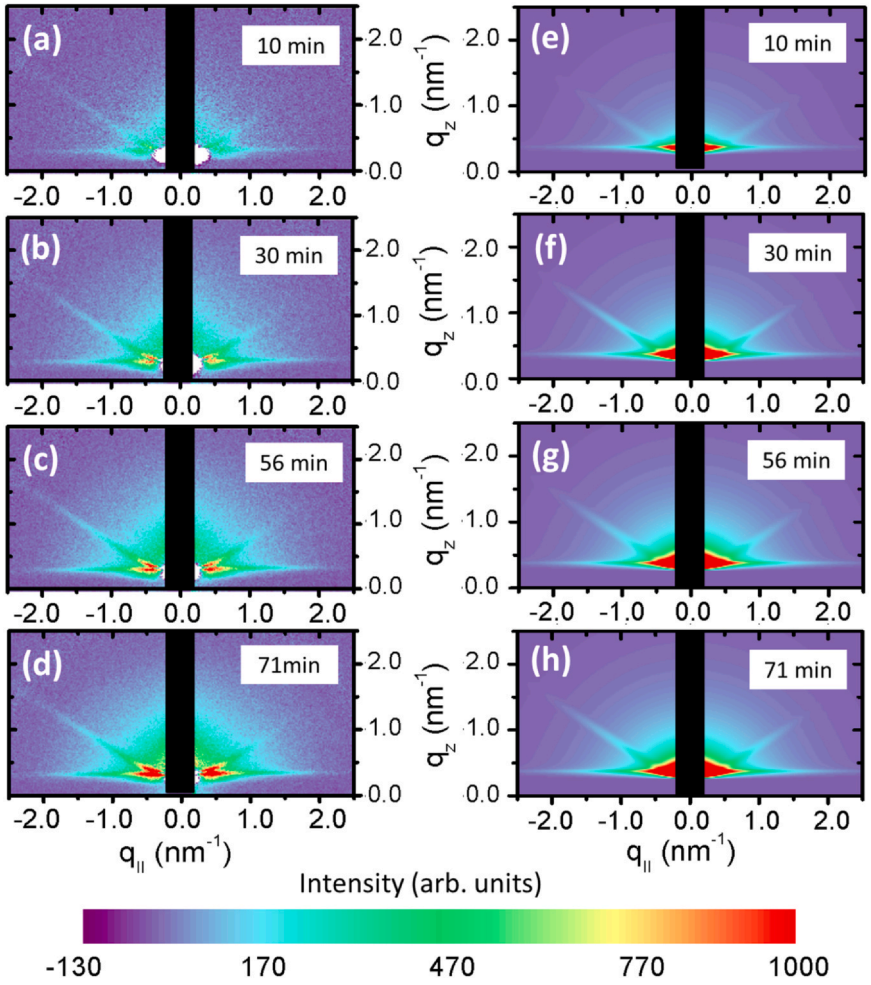

Fig. 3. Left column: Experimental 2D GISAXS intensity patterns of a Ni-doped SiO_2 thin film on Si(100) wafer during the thermal annealing at 405 °C for the indicated time periods. Right column: 2D intensity functions defined by Eq. (2) that best fit to the experimental intensity patterns. The isotropic component of the GISAXS intensity is produced by the scattering from spherical and randomly oriented Ni nanocrystals. The anisotropic components of the GISAXS evidenced by two narrow diagonal leaves are produced by thin hexagonal $NiSi_2$ nanoplates. The asymmetry of the two leaves is related to an offset of the azimuthal angle that was determined by the fitting procedure (ϕ = 1.0°). The vertical black stripe is the shadow of the primary beam stopper.

and orientation of the $NiSi_2$ nanoplates are preserved along the whole annealing process.

The anisotropic component of the total GISAXS intensity produced by $NiSi_2$ nanoplates buried in the Si wafer is rather weak as compared to the main isotropic part associated to the Ni nanocrystals dispersed in the SiO_2 thin film and in the corroded layer near the external surfaces of the Si wafer. For this reason, the results of the global fitting procedure were applied to determine only the time dependence of the radius distribution and number of Ni nanocrystals. Moreover, in order to determine the relevant size parameters associated to the $NiSi_2$ nanoplates, we have firstly subtracted the strong isotropic intensity produced by the nearly spherical Ni nanocrystals from the total scattering intensity and then analyzed exclusively the difference function.

We have plotted in Fig. 5 (symbols) four sets of 1D GISAXS experimental difference functions associated to different q_z values, each set corresponding to one of the indicated annealing times. The solid lines in Fig. 5 were calculated by the best fit procedure by applying Eq. (2) only including its last term which refers to the anisotropic component of the scattering intensity. From this analysis we have determined the time dependences of the average values of thickness $\langle\delta\rangle(t)$, maximum diameter $\langle D\rangle(t)$, dispersion in thickness and total number in arbitrary units $N_H(t)$ of $NiSi_2$ nanoplates.

5. Discussion

5.1. Kinetics of formation of Ni nanocrystals

The isotropic parts of the scattering intensity that is displayed in Figs. 3 and 4 are produced by nearly spherical Ni nanocrystals embedded in the deposited Ni-doped SiO_2 thin film and also inside an intermediate layer between the SiO_2 thin film and the Si layer in which the $NiSi_2$ nanoplates are located. The analysis of the isotropic components of the experimental GISAXS intensity was then conducted by fitting the first term in Eq. (2).

The results of our fitting procedure referring to the isotropic component of GISAXS intensity are displayed in Fig. 6(a), which shows the volume distribution of Ni nanocrystals for different times of thermal annealing. The two-mode feature of the volume radius distribution function, $V_{sph}(R, t) = (4\pi/3)R^3N(R, t)$, is clearly apparent in all plotted curves. From the results shown in Fig. 6(a), we have determined the time dependences of the volume distribution function of Ni nanocrystals for both populations (Fig. 6b). Since the GISAXS measurements were performed in arbitrary units, the values of $V_{sph}(R, t)$ and $V_{tot}(t) = \int V_{sph}(R, t)dR$ are also given in arbitrary units.

Our GISAXS experimental results clearly confirms the presence of spherical Ni nanocrystals as was previously seen in the STEM images of a previous work [1]. Analogously to the evidences shown in the

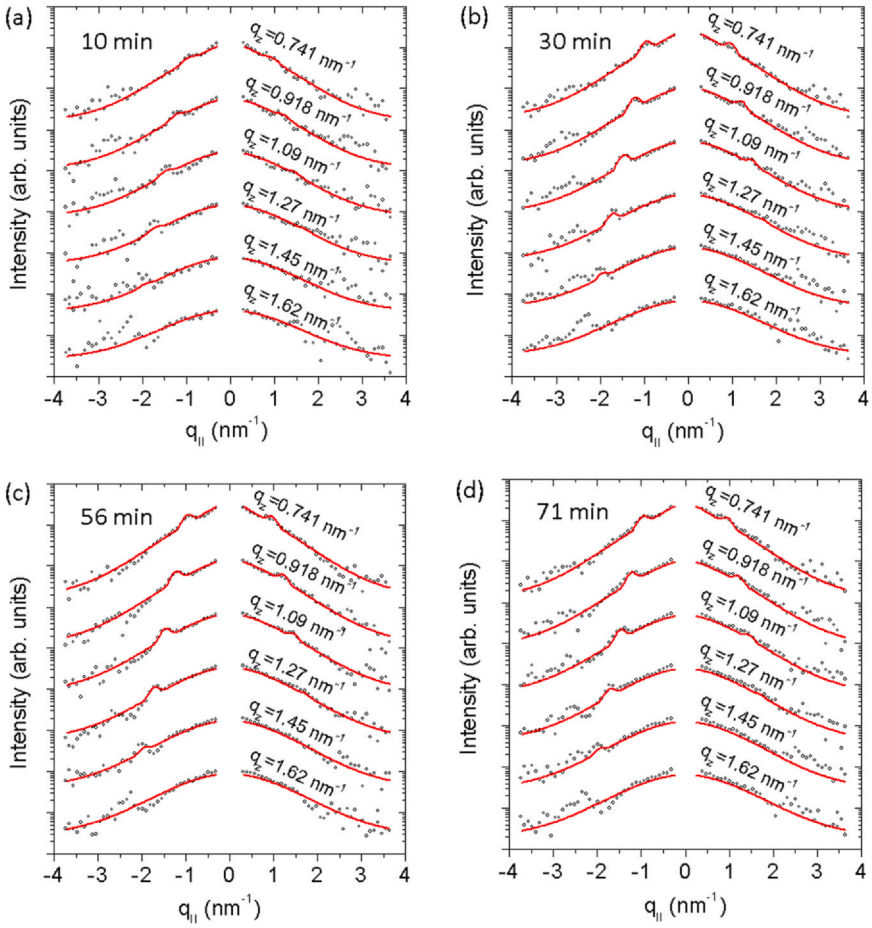

Fig. 4. Selected 1D GISAXS profiles $I(q_{||})$ for several q_z values corresponding to different periods of time of isothermal annealing, (a) 10 min (b) 30 min, (c) 56 min, (d) 71 min. The curves with symbols are the experimental profiles and the continuous lines are the calculated curves corresponding to the best fit of Eq. (2) to the experimental profiles. The curves in each figure are vertically displaced for clarity.

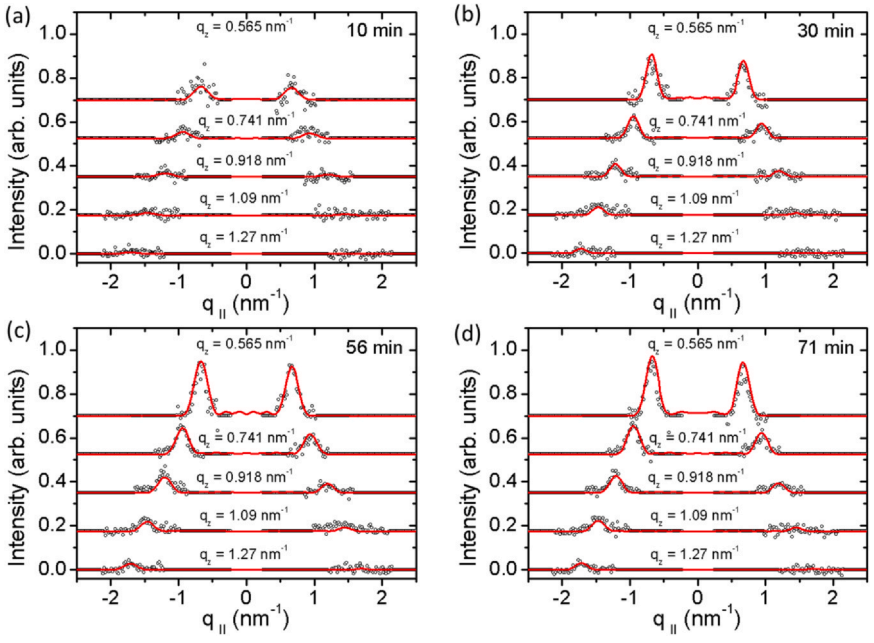

Fig. 5. Selected 1D GISAXS profiles, $I(q_{||})$, at different q_z values, after subtracting the isotropic component of the scattering intensity, corresponding to different periods of annealing time, (a) 10 min, (b) 30 min, (c) 56 min, (d) 71 min.

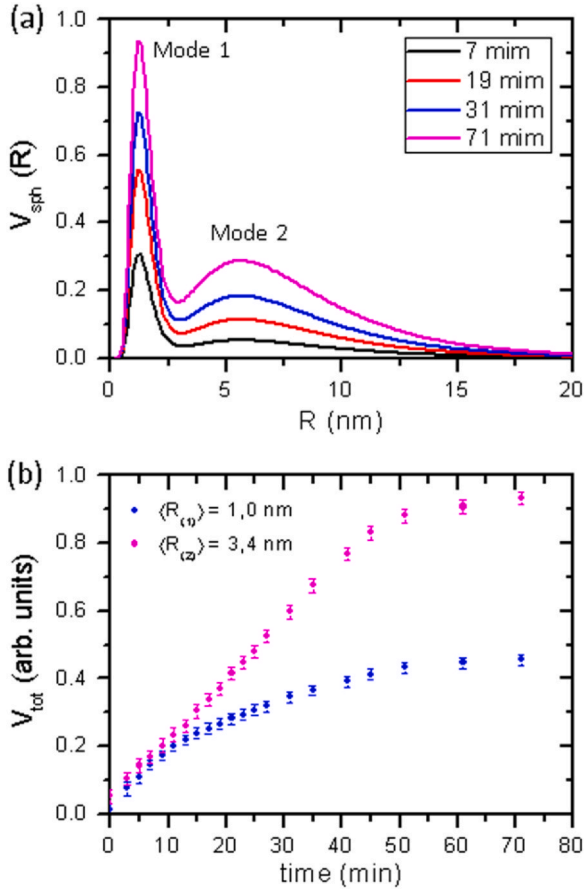

Fig. 6. (a) Several curves derived from GISAXS data displaying the volume weighed radius distribution functions of spherical Ni nanocrystals for the indicated times of isothermal annealing at 405 °C. Two radius modes are apparent; their average radii for all GISAXS curves being $\langle R_{(1)}\rangle$ = 1.0 nm and $\langle R_{(2)}\rangle$ = 3.4 nm. (b) Total volume of Ni nanocrystals for both nanocrystal populations as functions of the thermal annealing time.

previous STEM images [1], we assumed that the larger (mode 2) Ni nanocrystals are embedded in the nanoporous SiO_2 thin film and also located inside the Si wafer, in the intermediate layer (layer 2) close to its external surface, as schematically shown in Fig. 2. The intermediate layer consists of a Si matrix with irregular morphology associated to corrosion effects which produces a very high rugosity in the SiO_2:Si interface [1]. On the other hand, notice that the smaller (mode 1) Ni nanocrystals are not apparent in the STEM images shown in a previous article [1]. In this respect, we have assumed that the smaller (mode 1) Ni nanocrystals are located only inside the SiO_2 thin film and that they are progressively filling the small embedded nanopores. Notice that the features of the populations of Ni nanocrystals embedded in the SiO_2 thin film and those located in the Si intermediate layer are different. As a matter of fact, in the thin film there is a two-mode population (modes 1 and 2) while in the intermediate layer there is a one-mode population (mode 2). These different features are expected because of the significant differences of the host matrices in the nanoporous SiO_2 thin film (layer 1) and in the corroded intermediate layer of the Si wafer (layer 2).

The results plotted in Fig. 6(a) demonstrate that the values of the average radius and radius dispersion of both populations of nearly spherical Ni nanocrystals remain essentially invariant during the whole thermal annealing. The invariant average radii and radius dispersions of the population of smaller Ni nanocrystals (mode 1) are $\langle R_{(1)}\rangle = (1.0 \pm 0.1)$ nm and $\sigma_{(1)}/\langle R_{0(1)}\rangle = (0.35 \pm 0.05)$ and those of the population of larger Ni nanocrystals (mode 2) are $\langle R_{(2)}\rangle = (3.4 \pm 0.2)$ nm and $\sigma_{(2)}/\langle R_{(2)}\rangle = (0.5 \pm 0.1)$. The persistent increase in the isotropic contribution to the total scattering intensity for increasing annealing times was attributed to an increase in the number of Ni nanocrystals in Ni-doped SiO_2 thin film and in the intermediate layer.

Fig. 6(b) displays the $V_{tot(1)}(t)$ and $V_{tot(2)}(t)$ functions that describe the time dependences of the total volume of Ni nanocrystals for the populations with smaller and larger average radius, respectively. The slopes of $V_{tot(1)}(t)$ and $V_{tot(2)}(t)$ curves decrease for increasing times and these functions become essentially constant after 1 h of thermal annealing. Because of the progressive decrease in concentration of isolated Ni atoms in the silica thin film for increasing annealing times, the slowing down effect on the rate of volume growth is expected.

The observed invariances of the average radius and radius dispersion of the population of smaller Ni nanocrystals (mode 1) suggest that they nucleate inside the nanopores embedded in the SiO_2 film. On the other hand, the diffusion of Ni atoms is expected to be greatly enhanced by the interconnectivity of nanopores thus allowing for the fast growth of Ni nanocrystals. Thus, the final radii of the Ni nanocrystals are expected to be limited by the sizes of nanopores. The rate of growth of the volume of larger Ni nanocrystals (mode 2) is higher than that of smaller Ni nanocrystals (mode 1) formed inside the SiO_2 thin film. For larger nanocrystals (mode 2) the saturation of volume growth can be assigned to the consummation of Ni atoms in the host matrix.

5.2. Kinetics of formation of hexagonal $NiSi_2$ nanoplates

From the analysis of the profiles plotted in Fig. 5, exclusively related to the size, shape and orientations of the $NiSi_2$ nanoplates, we have determined the time dependences of the average thickness $\langle\delta\rangle(t)$ and maximum diameter of the hexagonal nanoplates $\langle D\rangle(t)$. The variations in intensity - measured in relative scale - provided additional information on the time dependence of the number of nanoplates in arbitrary units.

The time dependences of the average maximum diameter $\langle D\rangle(t)$ and thickness $\langle\delta\rangle(t)$ of the nanoplates are displayed in Fig. 7(a) and (b), respectively. For $t = 0$, i. e. at the starting of thermal annealing, the very weak GISAXS intensity evidences the initial absence of $NiSi_2$ nanoplates. Since the scattering intensity associated to the nanoplates for $t < 6$ min is very weak, the statistical quality of intensity data is poor and, for this reason, for early stages of annealing ($t < 6$min) the $\langle D\rangle(t)$ and $\langle\delta\rangle(t)$ functions could not be precisely determined. This evidences that the $NiSi_2$ nanoplates are formed and their sizes quickly increase within the first 6 min of thermal annealing. The curves displayed in Fig. 7(a) and (b) indicate that for higher annealing times no significant variations in $\langle D\rangle(t)$ and $\langle\delta\rangle(t)$ functions are apparent. The asymptotic values of the maximum diameter and thickness of the hexagonal $NiSi_2$ nanoplates are $\langle D\rangle = (62 \pm 4)$ nm and $\langle\delta\rangle = (8.5 \pm 0.5)$ nm, respectively. The $\langle D\rangle/\langle\delta\rangle$ aspect ratio remains nearly constant ($\langle D\rangle/\langle\delta\rangle \sim 7$) after the first 10 min of thermal annealing. The dispersion in the thickness of $NiSi_2$ nanoplates determined from the best fitting procedure was equal to 4 nm along the whole annealing time.

The time dependence of the total number of nanoplates $N_H(t)$, in arbitrary units, was also determined by fitting Eq. (2) to the experimental profiles shown in Fig. 5(a) to (d). The time dependence of the total volume of nanoplates $V_H(t)$ was determined also in arbitrary units using the relation $V_H(t) = \int_{\delta=0}^{\infty}(3\sqrt{3}/8)\langle D\rangle^2(t)\delta(t)N_{thick}(\delta, t)d\delta$. As shown in Fig. 7(c) and (d) both the number and total volume of nanoplates increase during the whole isothermal annealing, with a tendency to stability for $t > 50$ min. This evidences that nucleation of $NiSi_2$ nanoplates occurs over most of the annealing period, in all cases being followed by a very fast volume growth.

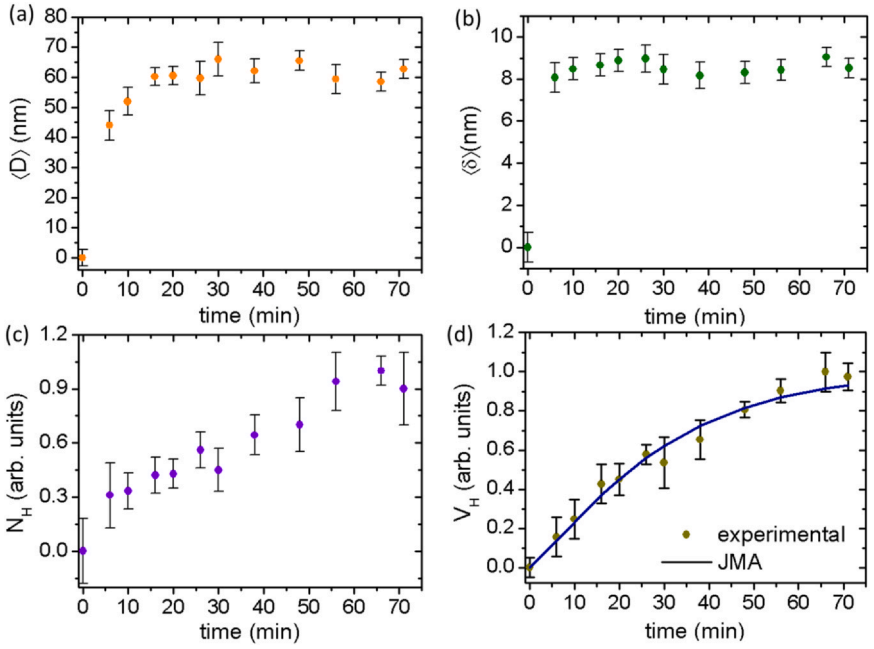

Fig. 7. Time dependences of relevant parameters derived from GISAXS data describing the formation and growth of $NiSi_2$ nanoplates buried in the Si(001) wafer during isothermal annealing at 405 °C. (a) Average maximum diameter $\langle D \rangle$, (b) average thickness $\langle \delta \rangle$, (c) total number $N_H(t)$ (in arbitrary units) and (d) total volume $V_H(t)$ (in arbitrary units). The solid line in (d) is the best fit of Johnson-Mehl-Avrami to the experimental $V_H(t)$ function.

Fig. 7(c) shows that during most of the annealing period the total number of $NiSi_2$ nanoplates $N_H(t)$ increases approximately linearly with time. This linear behavior is progressively slowing down and, for $t > 50$ min, the nanoplate number becomes approximately constant. This result is the expected consequence of the progressive decrease in concentration and consummation of Ni atoms dispersed in SiO_2 film. Notice that a similar effect is also apparent during the same period of annealing for the simultaneous formation of Ni nanocrystals in the deposited silica thin film and inside the Si(001) wafer (Fig. 6b).

The results described above show that $NiSi_2$ nanoplates reach their asymptotic size within a short time period ($t < 10$ min) while the nucleation of new platelets still takes place during a rather long additional period of time (1 h ca.). The reason why nanoplates stop growing after reaching an upper limit size is still an open question. Notice that the formation of additional $NiSi_2$ nanoplates long time after the end of the fast growth of those nucleated at $t = 0$ cannot be assigned to a decrease in concentration of Ni atoms dispersed in the thin film because, in this case, the depletion of Ni atoms would also leads to a decrease in the nucleation rate of silicide platelets. On the other hand, in some cases the stopping of growth of the nanoparticles in crystalline matrices is due to the development of strong strains associated to lattice mismatch [11]. However, since the difference in lattice parameters of Si and $NiSi_2$ at 405 °C is less than 0.01%, the strains developed during the growth of $NiSi_2$ nanoplates are not expected to be the major cause for stopping the growth process.

Furthermore, we have compared the experimental time dependence of the total volume of $NiSi_2$ nanoplates (Fig. 7d) with the prediction of Johnson-Mehl-Avrami (JMA) theory. According to JMA theory for isothermal phase transformations the following general relation holds [12–14]:

$$X_v(t) = \frac{V_0 - V_H(t)}{V_0 - V_\infty} = 1 - exp(-kt^n) \quad (3)$$

where V_0 e V_∞ are the initial and final total volumes of the nanoparticles, respectively, k is a constant related to the rate of formation of the new phase and n is an exponent depending on the particular mechanism and dimensionality of the phase growth process. The curve corresponding to the best fit of Eq. (3) to the experimental $V_H(t)$ function describing the time dependence of the total volume of $NiSi_2$ nanoplates is shown as a solid line in Fig. 7 (d). The exponent obtained from the best fitting procedure is $n = 1.18 \pm 0.05$. An exponent $n = 1$ is predicted by the JMA theory for a mechanism of diffusion-controlled growth leading to planar shaped precipitates when the distances between precipitates is much larger than their size [15]. These features agree with the geometrical features of the $NiSi_2$ thin nanoplates observed and characterized in this work. On the other hand, the fast formation of $NiSi_2$ nanoplates from the very beginning of thermal annealing - without an apparent incubation time - is a phenomenon expected for a process of heterogeneous nucleation [15], which is in accordance with previous results indicating that the formation $CoSi_2$ platelets endotaxially buried in a Si wafer starts preferentially at structural defects on the wafer surface [14].

6. Conclusions

In the presented work we have determined the time dependences of the parameters that rule the structural transformations under isothermal annealing at 405 °C of a composite material consisting of a single-crystalline Si wafer covered by a Ni-doped nanoporous silica thin film. In these structural transformations two simultaneous processes take place, namely (i) the formation of nearly spherical Ni nanocrystals inside a nanoporous SiO_2 thin film and in a thin layer of the Si wafer close to its external surface, and (ii) the formation of $NiSi_2$ thin nanoplates coherently buried in a Si wafer, with their large surface parallel to the planes of Si{111} crystallographic form.

Our results also demonstrated the formation of approximately spherical Ni nanocrystals with a two-mode radius distribution. Smaller nanocrystals are formed in the nanoporous SiO_2 thin film and larger ones inside the thin film and also in a thin layer close to the external wafer surface (layer 2). The average radii and radius dispersions of both populations of Ni nanocrystals are nearly invariant during the whole period of thermal annealing. We have determined that the invariant average radius and relative radius dispersions of the population of smaller nanocrystals are $\langle R_{0(1)} \rangle = (1.0 \pm 0.1)$ nm and $\sigma_{(1)}/\langle R_{0(1)} \rangle = (0.35 \pm 0.05)$ and those of the population of larger nanocrystals $\langle R_{0(2)} \rangle = (3.4 \pm 0.2)$ nm and $\sigma_{(2)}/\langle R_{0(2)} \rangle = (0.5 \pm 0.1)$. The observed invariance of the average radius and radius dispersion of Ni nanocrystals formed inside the SiO_2 thin film over the whole period of thermal annealing suggests that Ni nanocrystals nucleate inside the nanopores of the deposited silica film, their final sizes being limited by the sizes of the pores inside which they are formed.

We have also characterized the time dependent formation of hexagonal $NiSi_2$ nanoplates buried near the external surface of the Si(001) wafer, which occurs simultaneously with the formation of spherical Ni nanoparticles in the silica thin film and in the intermediate layer. Our analysis shows that the functions that describe the average thickness $\langle \delta \rangle$ and the maximum diameter $\langle D \rangle$ of the $NiSi_2$ nanoplates increase very rapidly during the first stage of annealing and reaches their final average values $\langle \delta \rangle = (8.5 \pm 0.5)$ nm and $\langle D \rangle = (62 \pm 4)$ nm after a period of 10 min ca.

Furthermore, the function that describes the total number of nanoplates in arbitrary units N_H increases during the first hour of thermal annealing while its rate of growth slows down for higher annealing times. The growth of $NiSi_2$ nanoplates stops shortly after their nucleation while the formation of new nanoplates is still going on, thus indicating that the maximum limit in the size of platelets cannot be related to a decrease in Ni concentration. The reason for this particular behavior remains unexplained and requires further investigation.

Finally, we have established that the time dependence of the total volume of $NiSi_2$ nanoplates agrees well with the prediction of the JMA theory for a model of two-dimensional diffusion-limited growth leading to a phase with a planar shape and thin thickness.

Declaration of Competing Interest

The authors declare that they have no known competing financial interests or personal relationships that could have appeared to influence the work reported in this paper.

Acknowledgments

Conselho Nacional de desenvolvimento Científico e Tecnológico - CNPq Processo 420781/2016-1, Pró-Reitoria de Pesquisa e Pós-Graduação-UFPR - Edital 004/2019 – Apoio a Atividades de Pesquisa – CPDCT/PRPPG/UFPR Processo nº 23075.044816/2019-95, LNNANO/CNPEM research proposal TEM-C1-25897, LNLS/CNPEM – research proposal XRD2-20180481, Project PICT-2015-2285 and PICT-2017-3150 (ANPCYT, Argentina), Project 11/X790 (UNLP, Argentina) and Project FINEP CT-INFRA 3080/2011.

Appendix A. Supplementary material

Supplementary data associated with this article can be found in the online version at doi:10.1016/j.jallcom.2021.160345.

References

[1] D.S. Costa, G. Kellermann, A.F. Craievich, L.A. Montoro, C.K. Oliveira, C.R.M. Afonso, C. Huck-Iriart, L.J. Giovanetti, F.G. Requejo, I.G. Zanella, I. Mazzaro, E.S. Szameitat, R.P. Cardoso, Highly oriented NiSi2@Si thin-nanocomposite produced by solid state diffusion: morphological and crystallographic characterization, 2021, (submitted for publication).
[2] A. Dahal, J. Gunasekera, L. Harringer, D.K. Singh, D.J. Singh, Metallic nickel silicides: experiments and theory for NiSi and first principles calculations for other phases, J. Alloy. Compd. 672 (2016) 110–116, https://doi.org/10.1016/j.jallcom.2016.02.133
[3] Y.C. Lin, K.C. Lu, W.W. Wu, J. Bai, L.J. Chen, K.N. Tu, Y. Huang, Single crystalline PtSi nanowires, PtSi/Si/PtSi nanowire heterostructures and nanodevices, Nano Lett. 8 (2008) 913–918, https://doi.org/10.1021/nl073279r
[4] W. Tang, B.M. Nguyen, R. Chen, S.A. Dayeh, Solid-state reaction of nickel silicide and germanide contacts to semiconductor nanochannels, Semicond. Sci. Technol. 29 (2014) 054004, https://doi.org/10.1088/0268-1242/29/5/054004
[5] P. Eaksuwanchai, K. Kurosaki, S. Tanusilp, Y. Ohishi, H. Muta, S. Yamanaka, Thermoelectric properties of Si-$NiSi_2$ bulk nanocomposites synthesized by a combined method of melt spinning and spark plasma sintering, J. Appl. Phys. 121 (2017) 225110, https://doi.org/10.1063/1.4985283
[6] N. Mingo, D. Hauser, N.P. Kobayashi, M. Plissonnier, A. Shakouri, Nanoparticle-in-alloy approach to efficient thermoelectrics: silicides in SiGe, Nano Lett. 9 (2009) 711–715, https://doi.org/10.1021/nl8031982
[7] N. Uchida, T. Tada, Y. Ohishi, Y. Miyazaki, K. Kurosaki, S. Yamanaka, Heavily doped silicon and nickel silicide nanocrystal composite films with enhanced thermoelectric efficiency, J. Appl. Phys. 114 (2013) 134311, https://doi.org/10.1063/1.4823814
[8] G. Kellermann, A.F. Craievich, R. Neuenschwander, T.S. Plivelic, Setup for in situ WAXS/SAXS studies of the formation and growth of Bi nanodroplets and the melting of Bi nanocrystals using synchrotron radiation, Nucl. Instrum. Methods Phys. Res. B 199 (2003) 112–116, https://doi.org/10.1016/S0168-583X(02)01422-2
[9] M. Tolan, X-ray Scattering from Soft-matter Thin Films, Springer-Verlag, Berlin, Heidelberg, 1999.
[10] R. Lazzari, IsGISAXS: a program for grazing- incidence small-angle X-ray scattering analysis of supported islands, J. Appl. Cryst. 35 (2002) 406–421, https://doi.org/10.1107/S0021889802006088
[11] P.A. Bennett, D.J. Smith, Z. He, M.C. Reuter, A.W. Ellis, F.M. Ross, In situ observations of endotaxial growth of $CoSi_2$ nanowires on Si(110) using ultrahigh vacuum transmission electron microscopy, Nanotechnology 22 (2011) 1–7, https://doi.org/10.1088/0957-4484/22/30/305606
[12] M. Avrami, Kinetics of phase change. I General theory, J. Chem. Phys. 7 (1939) 1103–1112, https://doi.org/10.1063/1.1750380
[13] M. Avrami, Kinetics of phase change. II, Transformation-time relations for random distribution of nuclei, J. Chem. Phys. 8 (1940) 212–224, https://doi.org/10.1063/1.1750631
[14] M. Avrami, Granulation, phase change, and microstructure kinetics of phase change. III, J. Chem. Phys. 9 (1941) 177–184, https://doi.org/10.1063/1.1750872
[15] J.W. Christian, The theory of transformations in metals and alloys, Pergamon, first ed., Union King, 2002.